Ultramicroscopy 243 (2023) 113629

Contents lists available at ScienceDirect

Ultramicroscopy

journal homepage: www.elsevier.com/locate/ultramic

Langmuir analysis of electron beam induced plasma in environmental TEM

J. Lindner [a], U. Ross [a], V. Roddatis [a,1], Ch. Jooss [a,b,*]

[a] Institute of Materials Physics, University of Goettingen, Friedrich-Hund-Platz 1, Goettingen 37077, Germany
[b] International Center for Advanced Studies of Energy Conversion (ICASEC), University of Goettingen, Goettingen D-37077, Germany

ABSTRACT

The characterisation of the gas state under electron impact is of high importance for the understanding of materials *in-situ* environmental transmission electron microscopy (ETEM) experiments. We report on the formation of a dilute plasma state of Ar and He based on the development of a Langmuir probe as a plasma diagnostic tool for the differentially pumped volume at the TEM sample position in the octagon. In order to keep stray magnetic field influences of the objective lens small, and thus the results readily interpretable within existing theory, the experiments are performed in Lorentz mode. The applicability of Langmuir type analysis for the identification of plasma parameters, such as ion density, plasma temperature, sheath extension and electron energy distribution is examined. The systematic study as a function of gas pressure and beam current reveals cold plasma characteristics with electron temperatures of around 0.4 eV and ion and electron densities that are orders of magnitude below the expected values from ionisation cross sections. The loss of charged particles appears to be due to surface collisions at the electrically conducting pole piece surfaces as well as at the conductive parts of the TEM holder.

1. Introduction

The interaction and reaction of gas and liquid environments with materials is an essential process in many topical areas such as electrochemical reactions, catalysis, interface and surface reactions as well as material nucleation and growth. In order to understand the underlying mechanisms, *in-situ* techniques in gaseous and liquid environments such as environmental X-ray photoemission spectroscopy [1–3], X-ray absorption spectroscopy [4], Raman spectroscopy [5,6], scanning electron microscopy [7,8] and TEM [9,10] have been developed. With respect to the ultimate goal of investigating the evolution of materials at atomic scale during reaction, *in-situ* TEM offers unique capabilities for real space and real time imaging of atomic processes as well as associated local analytic techniques down to Angstrom scales, using electron energy loss spectroscopy (EELS) and energy dispersive x-ray spectroscopy (EDX) [11]. This is a direct result of the adoption of aberration correctors [12–15]. Many *in-situ* capabilities are based on micro-electro-mechanical systems [16–23], which can provide a broad range of external stimuli. Furthermore, mass spectroscopy [24] and gas phase EELS allow the detection of gas composition as well as reaction products. The latter was predominantly achieved in closed liquid [25] and gas cells [26,27], since analysis of the change in gas composition in differentially pumped environmental TEMs (e-cell) is limited by the small volume fraction of the gas flow interacting with the sample material.

Many interesting effects have been observed in environmental TEM (ETEM) experiments in gas ambient. An important class of studies addresses shape changes of nanoparticles while catalysing CO oxidation [1] in the presence of atmospheric hydrogen pressure [2] and during oxidative etching [28]. Furthermore, size changes of model catalysts have been observed in air at elevated temperatures due to Ostwald ripening [29] as well as changes in chemical nanoparticle composition [30,31] and at surfaces [24]. Approaches to electrochemical studies in ETEM experiments in gas phase also involve the use of sacrificial reactions in order to reveal oxygen evolution [32], the study of electron beam induced electric potentials [33,34] and the correlation of changes in valence state to structural changes [35]. Recent studies compare stability and activity of manganite electrocatalysts for OER in ETEM water vapour experiments to cyclovoltammetry in liquid electrolytes, finding parallel trends of catalyst behaviour [36,37]. Atomic scale studies can access changes of surface termination as well as real time dynamics of atoms in the presence of gases [37–39]. They provide access to properties of gas–solid interfaces [22,24]. The comprehensive interpretation of these experiments requires an understanding of the state of the gas environment due to the impact of the electron beam.

Environmental TEM based on differential pumping possess a limited pressure range at the sample position from 10^{-7} up to 2000 Pa, where the upper limit is determined by the size of apertures used to maintain high-vacuum conditions in the rest of the column. In such systems the excellent spatial resolution is preserved [6,40,41]. Furthermore, the

* Corresponding author at: Institute of Materials Physics, University of Goettingen, Friedrich-Hund-Platz 1, Goettingen 37077, Germany.
E-mail address: jooss@ump.gwdg.de (Ch. Jooss).
[1] Present adress: Helmholtz-Zentrum Potsdam Deutsches GeoForschungsZentrum GFZ, Telegrafenberg, 14473 Potsdam, Germany

https://doi.org/10.1016/j.ultramic.2022.113629
Received 9 March 2022; Received in revised form 22 August 2022; Accepted 13 October 2022
Available online 15 October 2022

application of analytical techniques is straightforward, since no membrane windows are necessary to confine the environmental volume. Nevertheless, the state and properties of the ambient under electron beam impact are hardly understood. The beam interaction produces molecular and ionic species, secondary electrons and thus transfers energy into the medium. This may cause chemical side reactions and can alter reaction pathways. Based on the application of theoretical interaction cross sections, a rather small ionization ratio in the range of $5 \times 10^{-8} - 10^{-6}$ was estimated for He [33]. Nevertheless, depending on ionization rate and mean free path of electrons and ions, the gas may transform into a plasma state, i.e. ions and free electrons in the gas exhibit collective behaviour. This would imply that effects which are studied in the field of plasma catalysis need to be taken into account [42]. They include changes of stability and activity [43–45], creation of new active sites and modifications of the oxidation state of the exposed catalysts [46]. Furthermore, surface area enhancement and changes of the catalytic structure have been observed [47]. It has even been reported that changes of the plasma discharge type can arise [48]. Although conditions in conventional plasma catalysis are typically different from those in the ETEM experiments, the identification of possible effects of plasma interactions require a deeper understanding of the gas state under electron beam irradiation. Due to the inhomogeneity of the plasma generation by a localized electron beam in a large gas volume within the octagon, the theoretical prediction of even simple properties such as ion and electron densities is challenging and easily overestimates their magnitude. Thus, careful experimental studies are required.

Electron-beam generated plasmas are well known from the field of surface processing techniques [49], where they possess advantageous characteristics such as low electron plasma temperatures as well as ionization rates that may deviate from bulk plasmas. In these systems, electrons with energies of a few keV are used to generate plasmas in the low pressure range of ~1–3 Pa μ bar [50]. While some of the concepts of plasma generation and confinement of secondary electrons [51] in the sheath region of the electron beam can be transferred to our experiment, the radical difference in chamber dimensions and primary electron energy prohibits direct comparison.

Here, we apply a Langmuir plasma probe to the study of ionization properties in simple noble gases, i.e. He and Ar, under the impact of a continuous 300 keV electron beam. We select these gases since no complex chemistry of reaction products in the gas itself is involved and thus fundamental properties such as ion and electron densities, charge balance, formation and size of space charge layers, plasma temperature, mean free paths as well as kinetic energy distribution can be accessed as a function of gas pressure and electron flux. Since the Langmuir method is hardly established in the field of electron microscopy, we give a brief introduction into the self-constructed experimental setup and the theory with a critical review of its applicability in the Sections 2 and 3, respectively. In Section 4, the IV-curves recorded by the Langmuir probe are presented and analysed, using well-established plasma models in order to determine the appropriate sheath model of the plasma state. The orbital motion limited theory (OML) is applied to determine the charge carrier densities, plasma temperature and the resulting electron Debye lengths. The applicability of the OML theory is discussed in comparison to three complementary analysis methods for electron temperature determination in Section 5. This enables us to measure the plasma electron energy distribution. Based on the obtained experimental and theoretical results, we conclude that noble gases in ETEM under electron beam irradiation behave as a dilute plasma at pressures and electron dose rates relevant *in-situ* studies. Although the presence of a plasma sheath layer can be concluded from the Langmuir type of current voltage characteristics, the experimental magnitude of charged particle density seems to be strongly depleted compared to theoretical estimates from interaction cross sections by the presence of electrically conducting pole piece surfaces. The implications of the findings on the interpretation of ETEM experiments are discussed.

2. Langmuir probe analysis setup in the TEM

For plasma characterization a single wire Langmuir probe was constructed by modifying a single-tilt TEM holder. A hole was drilled through its body and an UHV-proof insulating ceramic tube was inserted. A Cu(-Mn) wire with a diameter of 250 μm was guided through the tube and vacuum-sealed with epoxy glue. The length of the outstanding bare probe was 5 mm. The tip was cut with a diamond saw and mechanically polished to obtain a smooth surface.

The single Langmuir probe measurements in the FEI Titan ETEM were performed in the Lorentz-SA mode in order to minimize the effect of magnetic fields. An illumination setting with a 1.8 μm diameter beam at the height of the Langmuir probe was used. The 300 kV electron beam was positioned at 20 μm distance from the tip end in order to exclude the direct contribution of beam tails to current measurements (Fig. 1b). Three different beam currents (I) were chosen at 5.5 nA, 8 nA, and 11 nA, as measured by the calibrated fluorescence screen. Reference current voltage (I-V) curves were recorded in high vacuum (1.8×10^{-5} Pa) with blanked and unblanked electron beams.

Argon and helium were chosen as working gases for the single electrode measurement, since they form a relatively simple plasma with one major species of single positive charged ions [52,53]. Monochromated electron energy loss spectroscopy was used to verify the ionization process. The according edges were 24.6 eV for helium and 15.75 eV for argon (S1 of the SI), consistent with literature.

Using noble gases without chemical reactions between generated ions simplifies the analysis. To reduce the residual water vapour fraction, the cold trap was LN_2-cooled during the experiments. The working

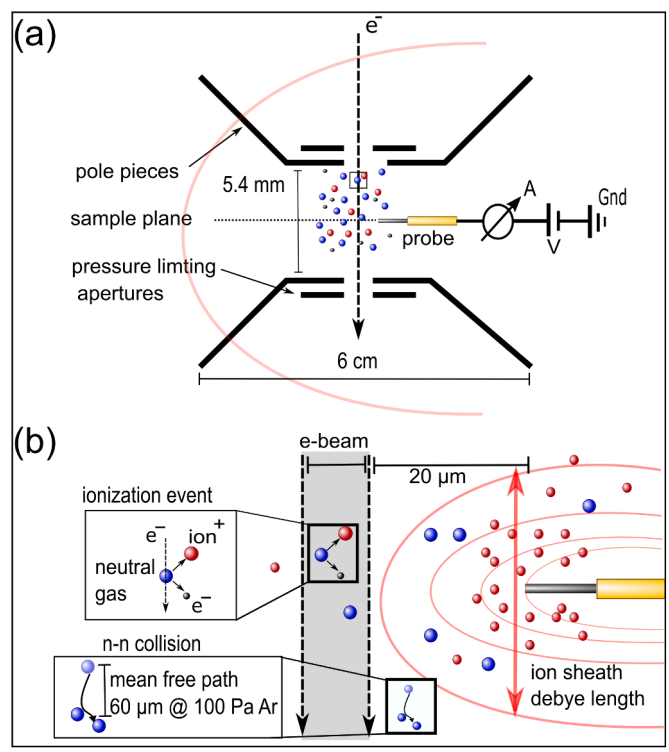

Fig. 1. Experimental overview of the Langmuir probe analysis of gas ionization state induced by the primary high energy electron beam. (a) Scheme of the geometry of gas volume between the pole pieces and the position of the Langmuir probe. The ion generation area is determined by the electron beam diameter of around 1.8 μm at near parallel illumination. The pole piece distance of 5.4 mm and diameter of the octagon are large compared to the neutral mean free path of around 60 μm at 100 Pa Ar. In contrast, ion and electron shielding lengths are comparable. (b) Magnified view showing the position of the electron beam with respect to the Langmuir probe. The latter has a length of 5 mm and is not drawn to scale.

gas purity (≳98%) of the column gas composition was verified with a residual gas analyser (mass spectrometer). In order to analyse the influence of pressure on the electron-beam induced ion density, the argon pressure was varied from 0.5 Pa up to 143 Pa and the helium pressure from 75 Pa to 510 Pa. I-V curves were also recorded for each pressure for reference. The probe voltage was ramped in 0.05 V steps via a Keithley 2601A sourcemeter in a voltage range from −6 V to +6 V, where both the ion- as well as the electron saturation regimes were observed in the Langmuir-curves. The current was measured with a Stanford SR570 current amplifier and its output voltage recorded with a DMM6500 with a conversion factor of 20 pA/V. After changing the bias voltage, a settling time of 4 s was allowed before taking 50 sampling points of the probe current.

3. Theory

3.1. Basic principles of Langmuir probe measurements

A plasma is a gas consisting a considerable fraction of free ions and electrons, which results in collective behaviour with the ability to screen charges. In the 1920's, Mott-Smith and Langmuir proposed an experimental method to analyse plasma properties. Their experimental setup consists of a single conductive probe which is inserted into the bulk of the ionized gas, which is referred to as a Langmuir Probe measurement [54]. It measures the electric current as a function of applied voltage with respect to the ground potential. The resulting I-V curve reveals three characteristic regimes (see Fig. 2), which enable the derivation of most important parameters of a plasma: The charge carrier-densities of ions and electrons, respectively, the mean electron temperature, the plasma potential and the plasma shielding length λ_D. For a floating probe, the net current is by definition zero. If such a conducting not grounded probe is inserted into a plasma, it will collect charges and built up an electric potential to maintain zero net current flow: For an increasing electron flux from the plasma to the probe, the probe potential will charge up more negatively. Thus, more ions from the surrounding volume are attracted, while the electron flux is reduced. Since the reverse processes apply for positive charging, a stable floating potential V_f is established. Typically, it is negative because the electron velocity exceeds the ion velocity [55].

If the probe bias is varied to sufficiently negative voltages ($V_B \ll V_f$), where electrons are repelled and ions are attracted, the probe draws the negative ion-saturation current $I_{i,sat}$

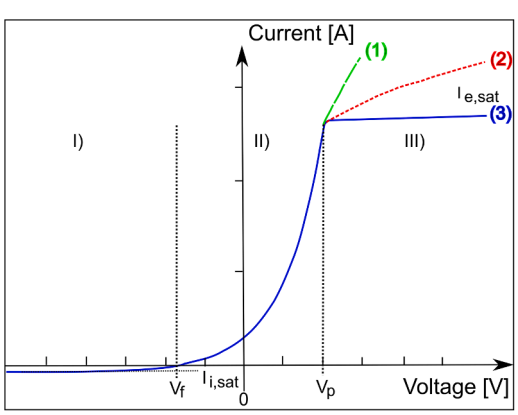

Fig. 2. Typical Langmuir single probe I-V-characteristics for a dense plasma: I) ion saturation regime, II) electron retarding regime III) electron saturation regime. The floating potential $\mathbf{V_f}$ and the plasma potential $\mathbf{V_p}$ are also shown. The latter indicated by a sharp change of the slope of the I-V curve. The I-V characteristics in the saturation regime depends on the sheath expansion and thus on the probe geometry: 1) spherical probe, 2) cylindrical probe, 3) ideal/guarded planar probe (reproduced from Ref. [56]).

$$I_{i,sat} = \exp\left(-\frac{1}{2}\right) e n_i \sqrt{\frac{k_B T_e}{m_i}} A_p,\ V_B \ll V_f \tag{1}$$

where e is the electron charge, n_i the ion density, k_B the Boltzmann constant, T_e the electron temperature, m_i the ion mass, and A_p the probe surface.

As the applied bias is gradually increased towards the floating potential, the high-energy fraction of the free electrons starts to contribute to the net current and partially balances it towards zero. Above V_f, the electron current overcomes the ion saturation current. The resulting electron retarding regime is described by an exponential growth of the measured current as a function of the applied bias by

$$I_e(V_B) = I_{e,sat}\ \exp\left(\frac{V_p - V_B}{T_e}\right),\ V_f < V_B < V_p \tag{2}$$

The measured current also depends on the electron temperature of the ionized gas, as described in Section 3.3. The electron retarding current saturates abruptly if the probe bias is equal to plasma potential V_p. At this specific voltage, the space charge sheath around the probe vanishes. The region of the I-V curve above the plasma potential ($V_B > V_p$) is thus called electron saturation regime. Inversely to the ion saturation regime, all ions are repelled and only electrons reach the probe. This results in the positive electron saturation current $I_{e,sat}$.

$$I_{e,sat} = e n_e A_p \sqrt{\frac{e T_e}{2\pi m_e}},\ V_B > V_p \tag{3}$$

Electron- and ion saturation regimes are only constant for planar probes and behave differently for other probe geometries as indicated in Fig. 2.

The quantitative analysis of the I-V curve of a Langmuir probe depends on several assumptions on the plasma state. First of all, it is assumed that the plasma has cold ions, i.e. $T_i/T_e \ll 1$. This is reasonable for electron impact ionisation, since the kinetic energy ratio of ions and secondary electrons reflects their mass ratio. The second assumption is that electrons are at or near thermal equilibrium, i.e. approximately follow a Maxwellian velocity distribution. This requires that the electron–electron scattering length is smaller than the mean free path governed by electron capture. We will provide evidence that this assumption is valid from the Druyvestyn analysis presented below. We further assume a collision-less plasma, i.e. the collisional mean-free path of plasma particles is larger than the spatial scale of interest, here the spatial extension of the plasma. Based on electron capture cross sections of the order of 10^{-20} m^2 both for Ar [57] and He [58], the related mean free path would vary between 4 m at 0.1 Pa and 4 mm at 100 Pa, thus, justifying this assumption. Furthermore, the analysis is restricted to an electrostatic plasma without ac stimulation and in the absence of a magnetic field. The assumption of a quasi-neutral plasma with $n_i \approx n_e$ that is isotropic and homogenous is valid if the mean free path of electrons and ions is of the same order of magnitude. Since the mean free path of both species is mostly limited by collisions of electrons and ions at the surrounding metal surfaces of the pole pieces, the validity of this criterion is assumed. We will return to the evaluation of the applicability of the Langmuir probe analysis in Section 5.3.

3.2. The plasma sheath

If an electrical conducting wire is inserted into a plasma, it will begin to draw a current until the balance of electron and ion flux is reached. Assuming a thermal plasma with the same mean energy of electrons and ions, the electrons have a higher mobility than the ions due to their lower mass. This leads to an accumulation of a net negative charge. The ions of the plasma are forming a positive charge cloud around the probe in order to shield this negative charge. The extension of the space charge cloud is determined by the electron Debye length.

$$\lambda_D = \sqrt{\frac{\varepsilon_0 k_B T_e}{e^2 n_e}} \tag{4}$$

The spatial extend of the generated electric field around the probe is thus limited by the sheath diameter, given by the electron Debye length. Compared to the bulk plasma, the electron and ion-densities are both reduced, but not with the same rate: Near the probe at a distance below λ_D, the electron density diminishes faster than the ion density [56].

In the following, we will show that the extension of the sheath layer λ_D in the ETEM exceeds the wall distance in the pole piece gap. Consequently the Langmuir probe measures a charge-carrier depleted state within the extended double sheath in the pole piece gap.

Comparing the magnitudes of $I_{e,sat}$ and $I_{i,sat}$ for the above equations results in:

$$I_{e,sat} = -exp\left(\frac{1}{2}\right) I_{i,sat}\sqrt{\frac{m_i}{(2\pi m_e)}} \approx \begin{cases} 180\ I_{i,sat}, & \text{Ar} \\ 56\ I_{i,sat}, & \text{He} \end{cases} \tag{5}$$

In real experiments, an increase of the bias voltage above the plasma potential does not keep the saturation current constant. Under these circumstances, the collected current is no longer exclusively determined by the physical surface area of the probe. The sheath expands with increasing bias, leading to an effectively enlarged current collection area. The increase of the measured current due to sheath expansion for three probe geometries is drawn in Fig. 2. The electron saturation current can be still extracted from probe current at the plasma potential, since at this bias voltage no sheath layer and therefore no sheath expansion is present. The sheath expansion also takes place in the ion saturation regime $V_B \ll V_f$. In order to extract the charge carrier density from this regime, the ion saturation current has to be corrected based on a sheath model and according to the probe-geometry. The choice of the sheath correction model thus depends on the ratio of the probe radius r_p to the Debye length λ_D. We have verified different sheath correction models and concluded from our findings that with a probe radius of r_p= 250 µm and Debye lengths in the range of $\lambda_D =$ 8–100 mm (Ar) and 30–300 mm (He), the application of a thick sheath approximation based on the orbital motion limited model is most reasonable. However, the confined geometry of the plasma in a pole piece gap smaller than λ_D implies that the sheath models must be applied with care.

3.3. Orbital-motion limited thick sheath

The orbital-motion limited (OML) sheath model [54,59,60] derives the ion collection current for a thick sheath with a smooth and slow potential variation from $V_\infty = 0$ to the negative probe potential V_B. It assumes cold ions (T_i / $T_e \ll 1$), which are Maxwellian distributed and approach the probe with a one directional velocity v_0 at a large distance. Under these assumptions the OML electron current can be expressed according to Allen et al. [59] as

$$I(V_B) \approx 2\pi n_0 r_p \cdot \left(\frac{k_B T}{2\pi m_e}\right)^{1/2} \frac{2}{\sqrt{\pi}} \left(1 + \frac{eV_B}{k_B T_e}\right)^{1/2} \tag{6}$$

While the ion current is given by

$$I_{OML,i}(V_B) \approx 2\pi n_0 r_p \cdot \frac{\sqrt{2}}{\pi} \left(\frac{e(V_P - V_B)}{m_i}\right)^{1/2} \tag{7}$$

In the orbital motion limit the ion current does not saturate and does not depend on the electron temperature T_e. Therefore in the OML limit $I^2(V_p\text{-}V_B)$ is a linear function and the ion density can be found under the conditions $\frac{e(V_p - V_B)}{k_B T_e} \gg 1$ and $\frac{r_p}{\lambda_D} \lesssim 3$ [61] by evaluating the slope:

$$n_0 \approx \frac{\pi}{A_p} e^{-3/2} \sqrt{2m_i} \left[-\frac{dI^2}{dV}\right]^{1/2} \tag{8}$$

4. Results

Since the applicability of Langmuir analysis on the experimental results depends on the plasma parameter, one needs to iterate the analysis and confirm the validity of the assumptions. Furthermore, the effect of the special geometry of the plasma in the ETEM must be analysed. This includes the small generation volume of the plasma in the interaction area of the primary electron beam with gas atoms, the presence of close-by electrically conducting walls at the pole pieces and the presence of a metal frame with a bias voltage of +2 V. The latter is typically used to detect accidental contact of the TEM sample holder to the pole piece. In the following, we demonstrate that the electron-beam induced plasma properties fit the expectations from Langmuir theory, if carrier depletion by close by pole piece surfaces is considered. We select suitable approximations, and derive accessible parameters.

4.1. Pressure and current dependent IV curves

Fig. 3 shows the Langmuir-type of measurements of IV-traces that were recorded as a function of pressure of the Ar and He working gases and electron beam illumination. The measurements in high-vacuum yield zero current, independently of whether the electron beam was blanked or not. The same applies for measurements in gas environment with a blanked electron beam. In gas and under electron beam

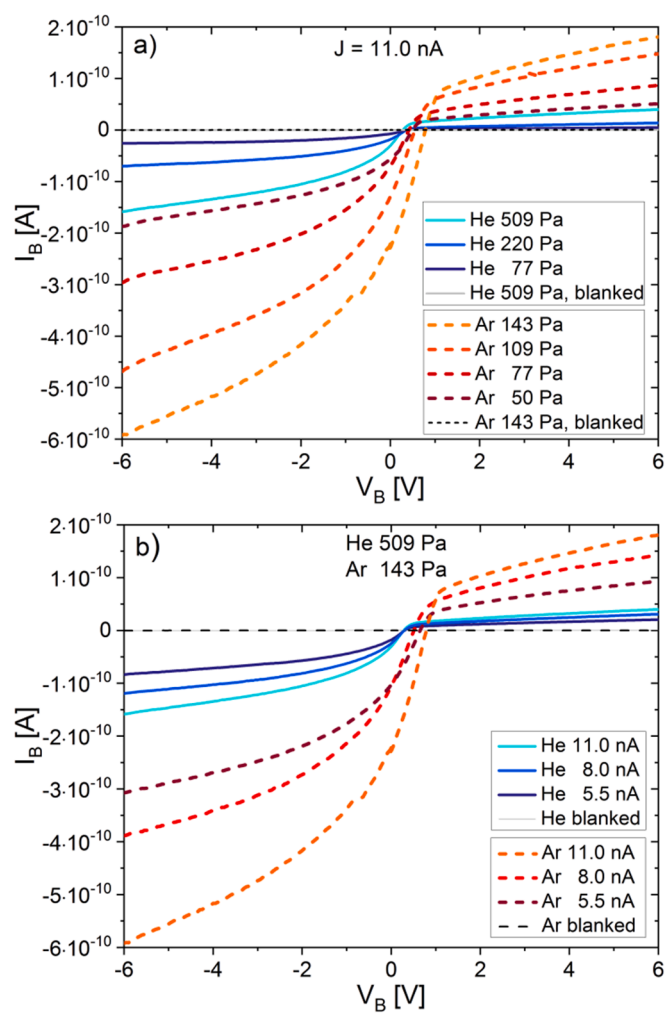

Fig. 3. Langmuir probe measurements in the ETEM at different gas pressures and beam currents. (a) Pressure variation at constant beam current of 11 nA for Ar (dashed) and He (solid). (b) Beam current dependence at constant pressure of 143 Pa for Ar and 509 Pa for He.

ionization, currents of up to several hundred pA in both biasing directions were obtained. Both gases show the same general curve shape. The measured current increases with the gas pressure: At the same conditions, e.g. for 11 nA beam current and 77 Pa gas pressure, the maximum current in Ar is greater than in He. A similar qualitative behaviour is observed for the variation of the beam current at constant gas pressure: the magnitude of the measured current increases with increasing beam current.

4.2. Classification as a plasma: general considerations

Fig. 4 shows the I-V-curves for He and Ar, respectively, at a beam current of 11 nA and similar pressures. The inset shows the first derivative of both curves. It exhibits the characteristic features predicted by Langmuir-plasma theory: an ion saturation regime, the exponential growth indicating the electron retarding regime and the electron saturation regime for cylindrical probes (compare with Fig. 2). The plasma potential can be associated with the peak in the first derivative. At this point the electron retarding regime transforms into the cylindrical sheath expansion regime. Even without additional smoothing, the maxima are easy to locate and result in V_p (Ar, 11 nA, 70 Pa) = 0.35 V and V_P (He, 11 nA, 500 Pa) = 0.2 V.

As one would expect, both types of saturation currents are greater for argon than for helium due to the difference in ionization cross-section. The Langmuir theory would predict a ratio of $I_{e,sat}/I_{i,sat}$= 180 for Ar and 56 for He; see Eq. (5). However, in our measurements, the ion saturation current seems to exceed the electron saturation current by a factor of 3 for both noble gases. This surprisingly small electron saturation current is connected to the observed positive floating potential. We find that V_f is 0.1 V above the plasma potential. In a conventional Ar bulk plasma with $T_e = 2$ eV and $n_0 = 10^{16}$ m^{-3}, one would expect the floating potential to be a few Volts negative, while the plasma potential is expected at 1 V [55]. Indeed, the measured current at the plasma potential is still negative, i.e. an ion current. This indicates that a significant fraction of the fast electrons is removed by the walls and the biased frame of the TEM holder. Another possible origin of deviations from the expected $I_{e,sat}/I_{i,sat}$ ratio in plasma experiments are magnetic field effects [60,62]. Since the analysis of these effects requires the determination of plasma parameters such as the Debye length, this topic will be further discussed below.

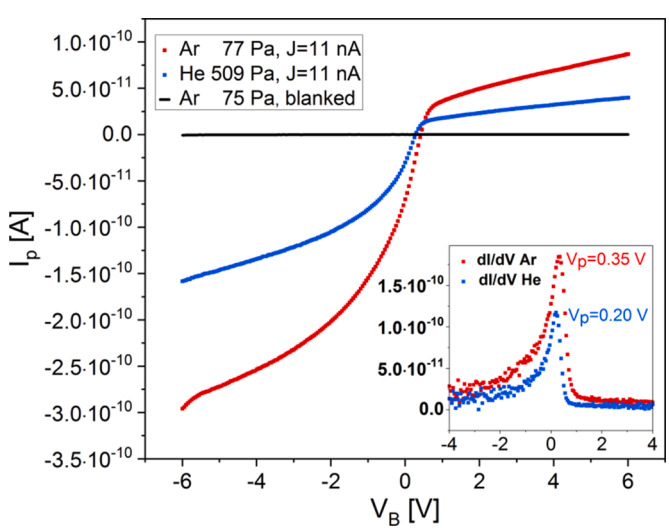

Fig. 4. IV-curves measured by a single probe Langmuir-TEM holder in Lorentz-mode at pressures of 76.8 Pa for Ar and 509 Pa for He. A beam current of 11 nA is compared to a blanked beam. The inset shows the first derivative of the data. The sharp maximum indicates the plasma potential.

4.3. Electron temperature

The choice of the sheath model is done in two separate steps: First, the electron temperature is extracted from the electron retarding regime. Here, the probe current $I_B(V_B)$ still contains an ion-current contribution, which needs to be removed. Therefore, a preliminary ion-saturation fit is carried out with a linear regression and the fit is subtracted from the measured probe current. After taking the natural logarithm of the residual electron current, the linear region in the electron retarding regime is analysed with a second regression. The inverse slope of this second regression allows the determination of the electron temperature (see Fig. 5a). Results for T_e of He and Ar are compared in Fig. 5b.

4.4. Choice of the sheath model

In order to select the appropriate ion-sheath model, the electron Debye length must be calculated from the I-V-trace. A limiting-case estimate was carried out in order to show that all measured curves belong to the thick sheath OML-regime. The upper limit for the r_p/λ_D ratio is obtained if the smallest electron temperature and the highest charge carrier density are used as previously determined. The electron density

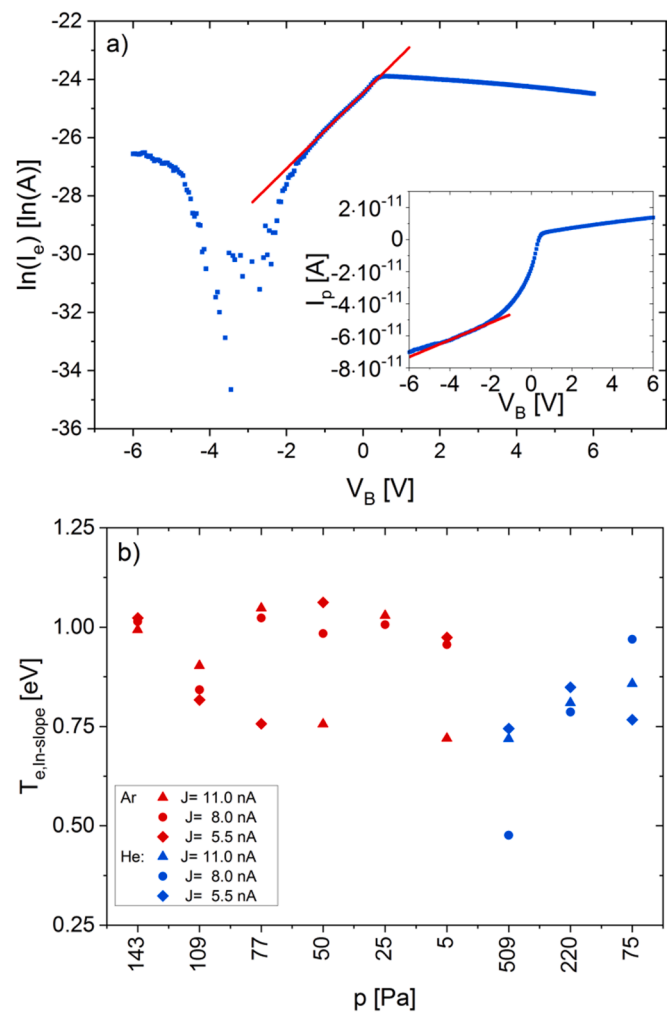

Fig. 5. (a) Typical linear regression of $\ln(I_e(V_B))$ in order to determine T_e from the electron retarding region. A typical example is shown for a He pressure of 220 Pa and a beam current of 11 nA. Inset: linear ion-saturation regression for the same conditions. (b) Resulting electron temperatures determined from the logarithmic derivative of the I-V curve in the electron retarding regime (see text).

Table 1
Determined limiting-case values for the parameters ion density $n_{i,max}$, electron density $n_{e,max}$, Debye length $\lambda_{D,max}$ and resulting r_p/λ_D ratios. Here, r_p denotes the tip radius of the Langmuir probe. The given values refer to $I = 11$ nA, for pressures of $p = 143$ Pa for Ar and $p = 510$ Pa for He, respectively.

Argon				
$T_{e,min}$ [eV]	$I_{i,max}(-6\ V)$[A]	$n_{i,max}$ [m^{-3}]	λ_D [m]	r_p/λ_D
0.75	$-5.92\cdot10^{-10}$	$8.33\cdot10^{11}$	$8.95\cdot10^{-05}$	$2.23\cdot10^{00}$
$T_{e,min}$ [eV]	$I_{e,max}(+6\ V)$[A]	$n_{e,max}$ [m^{-3}]	λ_D [m]	r_p/λ_D
0.75	$1.81\cdot10^{-10}$	$1.44\cdot10^{09}$	$2.16\cdot10^{-03}$	$9.62\cdot10^{-02}$
Helium				
$T_{e,min}$ [eV]	$I_{i,max}(-6\ V)$[A]	ni,max [m^{-3}]	λ_D [m]	r_p/λ_D
0.50	$-1.58\cdot10^{-10}$	$3.00\cdot10^{11}$	$1.10\cdot10^{-04}$	$1.56\cdot10^{00}$
$T_{e,min}$ [eV]	$I_{e,max}(+6\ V)$[A]	$n_{e,max}$ [m^{-3}]	λ_D [m]	r_p/λ_D
0.50	$3.99\cdot10^{-11}$	$4.27\cdot10^{08}$	$2.16\cdot10^{-03}$	$5.89\cdot10^{-02}$

is intentionally overestimated by using the maximum measured current at $I_p(+6\ V)$ and analogous for the ion current $I_p(-6\ V)$, since the sheath expansion regimes are already reached at ±6 V.

The limiting-case estimate in Table 1 shows that all I-V-traces have to be treated with the thick-sheath-OML approximation in equations (6) since $r_p/\lambda_D \ll 3$. It is important to note that in the OML assumption for cylindrical probes, the ion density calculation is independent of the electron temperature and that the ion saturation regime is not sensitive to residual magnetization.

4.5. Ion density extraction

After the determination of the sheath thickness and the selection of the appropriate OML model, the ion concentrations in both noble gases can be determined in dependence of beam current and pressure. The analysis is carried out by applying Eqs. (7) and (8). Examples of fits for both gas types are shown in Fig. 6.

From this analysis, it becomes apparent that the OML ion density scales linearly with pressure and beam current, respectively, for both noble gases. The plot of the resulting ion density as a function of the product of both parameters is shown in Fig. 7.

4.6. Debye length

As discussed in Section 4.2, the ion density can be determined with a higher confidence from the ion saturation current than the electron density. The ion density is thus used as the value for the charge carrier density both for ions and electrons, under the assumption of charge neutrality. For the electron temperature, we use two limits that were obtained from the logarithmic derivative of the I-V curve in the electron retarding regime (also called ln-slope method) and the OML model, respectively. The resulting Debye-lengths λ_D are presented in Fig. 8. For both limits, the obtained λ_D values have the same order of magnitude and range from centimetres for low pressures and beam currents to several millimetres for the highest ones.

Since the obtained Debye-lengths are larger as or of the order of the geometric distance of the plasma walls, given by the pole piece distance of 5.4 mm, the assumption of a bulk plasma is not valid. Consequently, the determined charge carrier densities do not represent the bulk carrier densities. They are affected by the charge attachment at the pole piece surfaces leading to the formation of space charge layers.

4.7. Druyvesteyn analysis: electron energy distribution

The Langmuir theory is derived for a thermal plasma, where the electron energy distribution function (EEDF) is Maxwellian. Therefore, in the following, this requirement for the analysis of the ETEM plasma is verified. The EEDF f(ϵ) can be reconstructed from the Langmuir-IV-trace by application of the Druyvesteyn formula. It uses the second derivative of the probe current with respect to the bias below the plasma potential [63]:

$$f(\in = V_B - V_p) = \frac{2}{e^2 A_p}(2m_e e\ \in)^{\frac{1}{2}}\frac{d^2 I}{dV^2} \tag{9}$$

Since the second derivative of the probe data is very sensitive to noise and plasma fluctuations, we have used a Savitzky-Golay filter to smooth the initial data. A typical result for Ar at 11 nA beam current and 109 Pa gas pressure is shown in S2 of the SI. The EEDF is then reconstructed by expressing the probe bias relative to the plasma potential

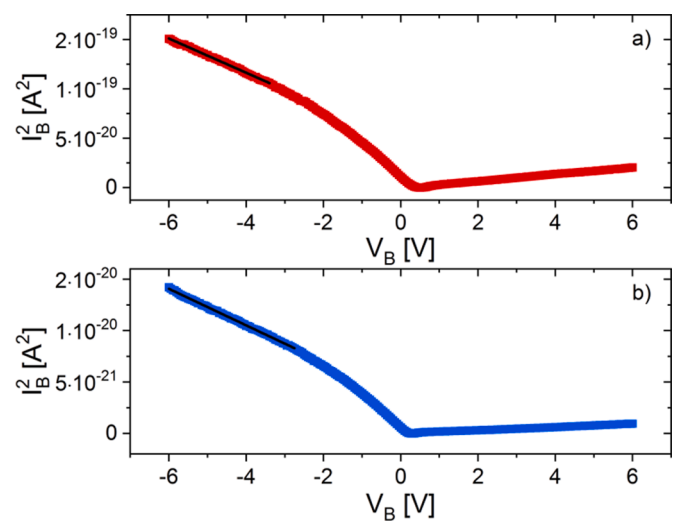

Fig. 6. Ion saturation fits according to OML theory shown for Ar (a) and He (b) at 8 nA beam current and pressures of 143 Pa and 500 Pa, respectively.

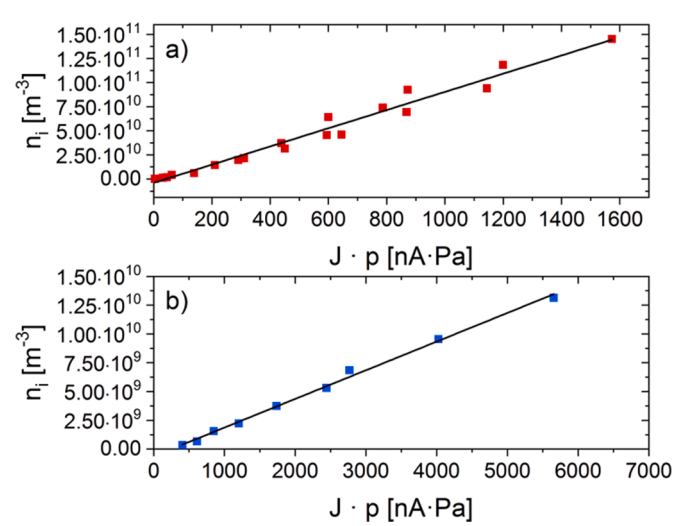

Fig. 7. Linear fit of the determined ion densities from OML theory, in dependence of the product of beam current and pressure for Ar (a) and He (b).

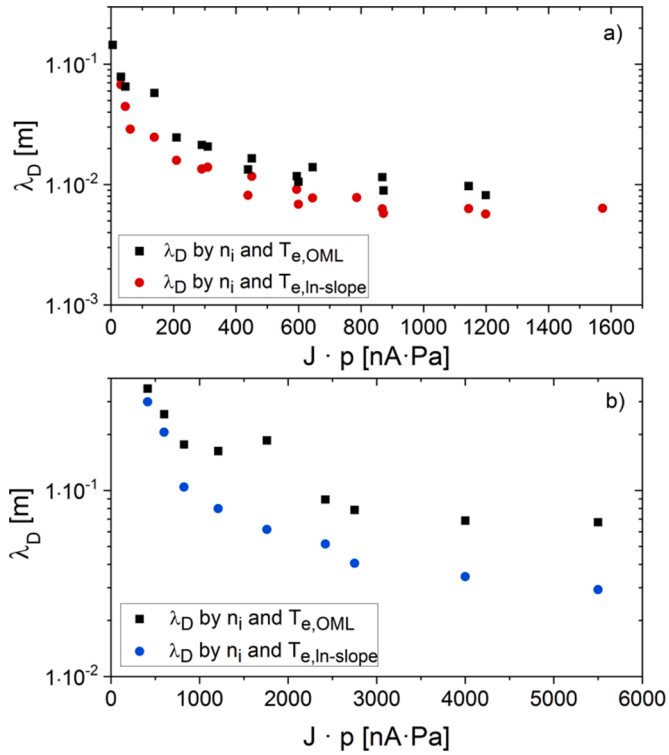

Fig. 8. Debye screening lengths for Ar (a) and He (b). The two sets of values are calculated by using the ion density and two limits for T_e derived from the ln-slope method and the OML model.

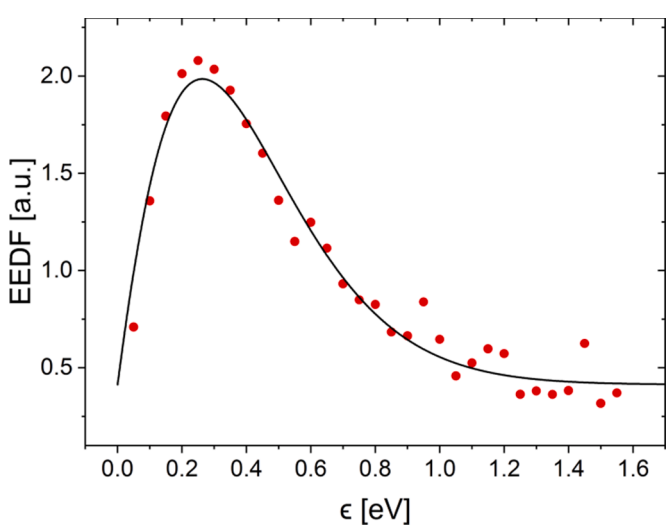

Fig. 9. Electron energy distribution function (EEDF) exemplarily shown for Ar at a beam current of 8 nA and pressure of 109 Pa. The EEDF-fit is carried out according to the generalized Gudmundssen model.

and applying the Druyvesteyn formula (9). The result is shown in Fig. 9.

The Druyvesteyn energy distribution of electrons in plasmas is a generalisation of the Maxwellian distribution. It takes deviations due to inelastic collisions, wall effects and non-negligible magnetic fields, as well as anisotropic ion velocities [61] into account. It reflects that the high energy fraction of the electrons can be depleted, compared to the Maxwellian EEDF. Gudmundssen et al. [64] provide an EEDF model that covers the transition regime between Maxwellian ($x = 1$) and Druyvesteyn ($x = 2$) distributions via intermediate distributions ($1<x<2$).

The generalized model was used to fit the obtained noble gas EEDFs in the ETEM with the parameters $a, b, \langle\in\rangle$ and x according to

$$f(\in) = a\left[\frac{x}{<\in>^{\frac{3}{2}}}\frac{[\Gamma(\xi_2)]^{\frac{3}{2}}}{[\Gamma(\xi_1)]^{\frac{5}{2}}}\in^{\frac{1}{2}}\exp\left(-\frac{1}{<\in>^x}\left[\frac{\Gamma(\xi_2)}{\Gamma(\xi_1)}\right]^x\in^x\right)\right]+b$$

$$T_e = \frac{3}{2}k_B\langle\in\rangle, \tag{10}$$

$$\xi_1 = \frac{3}{2x},\ \xi_2 = \frac{5}{2x},\ \Gamma(\xi) = \int_0^\infty t^{1-\xi}\exp(-t)dt$$

Although Gudmundssen et al. point out that their generalized model is not suitable to yield reliable plasma parameters, it is possible to use this model to verify the Langmuir condition of the ETEM plasma. Therefore, the quantification of the type of EEDF by the exponent x and the adjusted R^2 is shown in Fig. 10. It indicates that the EEDF is Maxwellian type ($x = 1$) within the 95%-confidence interval for He and, except for the highest beam currents, for Ar. Thus, the further use of the Langmuir theory is justified for most experimental parameters.

5. Discussion

5.1. Evaluation of T_e by different methods

The electron temperature was determined by three different methods available to Langmuir probing, as shown in Fig. 11.

Druyvesteyn method: The electron density and electron temperature can be derived by the Druyvesteyn-method in the electron retarding regime once the EEDF is obtained. Following the fitting procedure in Section 4.7, the fits are used to determine the electron temperature according to [61]:

$$n_e = \int_0^\infty f(\in)d\in \tag{11}$$

$$T_e = \frac{2}{3n_e}\int_0^\infty \in\cdot f(\in)d\in \tag{12}$$

Evaluating Eqs. (11) and (12), there are three reasons why one might expect a lower resulting electron temperature. First, the method would require an appropriate subtraction of the nonlinear ion current. Since this was not possible, the resulting charge carrier density is too high. Second, the integration is limited to the fitted regime with energy range <1.5 eV and therefore one expects a slightly underestimated electron temperature as well. Third, the fraction of the secondary electrons that are generated in the interaction zone of the primary electron beam with the gas with $E \gg T_e$, as visible in the electron energy loss spectra in Fig. S1 in the SI, might be invisible in the probe current. This is due to the rapid drop of the EEDF towards higher energies.

OML model: Within the OML-sheath model, the electron density is determined by the slope of the $I^2(V_B)$-dependency in the electron saturation regime according to Eq. (6). Subsequently, the electron temperature can be calculated by the fit-intercept with:

$$T_e(OML, esat) = V_p + Intercept\cdot\frac{\pi^2 m_e}{2n_e^2 A_p^2 e^3} \tag{13}$$

The obtained intercept is negative, and thus the calculated electron temperatures are smaller compared to applying the ion saturation regime. Therefore, T_e calculated from the electron saturation regime within OML is underestimated.

Ln-slope method: The determination of the electron temperature using the natural logarithm of the I-V curve in the electron retarding regime requires the subtraction of the ion current. Since the electron current is reduced, the assumption that in the electron retarding regime $I_{probe} \cong I_e$ may not hold. Therefore the determination of the electron temperature via the slope of $\ln(I_e)$ would require a more careful ion

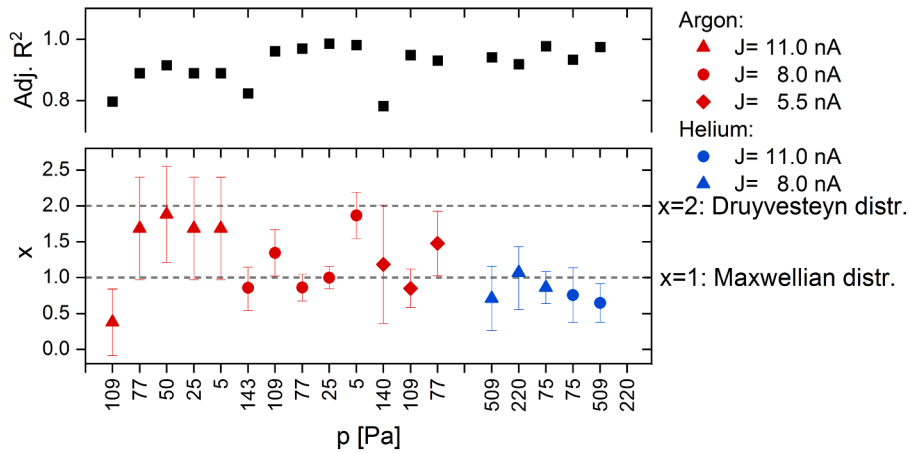

Fig. 10. Results of the EEDF-fits according to the generalized Gudmundssen model. The distribution type factor x with its 95%-confidence intervals as well as the corresponding adjusted quality factor R^2 are shown for Ar and He.

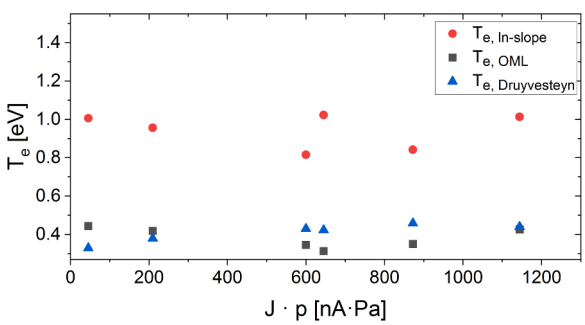

Fig. 11. Determination of the electron temperature in Ar using three different methods: Analysis of the electron saturation regime according to the OML model, calculation of the electron temperature via first moment of the generalized Gudmundssen fits and the logarithmic derivate of the I-V characteristic in the electron retarding regime, i.e. ln-slope method.

current subtraction than as usual. A linear subtraction of the ion current was performed, as suggested in [61]. This might be an oversimplification since the ion current should decrease when the probe bias approaches the plasma potential. Consequently, it can be assumed that the linear ion correction leads to an underestimate of the derived slope and an overestimate of the electron temperature.

In conclusion, due to the uncertainties of all evaluation methods, only upper and lower limits for the electron temperature are given. We suggest that the lower limit is determined by the outcome of the Druvestyn analysis, as well as the result from the electron saturation regime via OML. The upper limit is given by the result of the ln-slope method. The results of all three methods may be affected by the residual magnetic field that is present at the position of the Langmuir probe despite using the Lorentz mode. Notably, the lower values of $T_e \leq 1$ eV are close to previously reported plasma parameters from keV electron beams [50].

5.2. Wall effects

It is possible to investigate the influence of the nearby conducting surfaces of the pole pieces by removing the frame of the modified TEM holder. This frame, as well as the TEM sample holder body, is biased to a voltage of +2 V vs. ground. Since the plasma and ion behaviour under *in-situ* ETEM conditions typically for the study of catalytic specimens is of interest, most of the data is taken with the frame in place. The plasma I-V curves with and without frame are compared in Fig. 12. It is observed that both the plasma and the floating potentials are shifted to negative values. In addition, a steeper current increase in the electron retarding

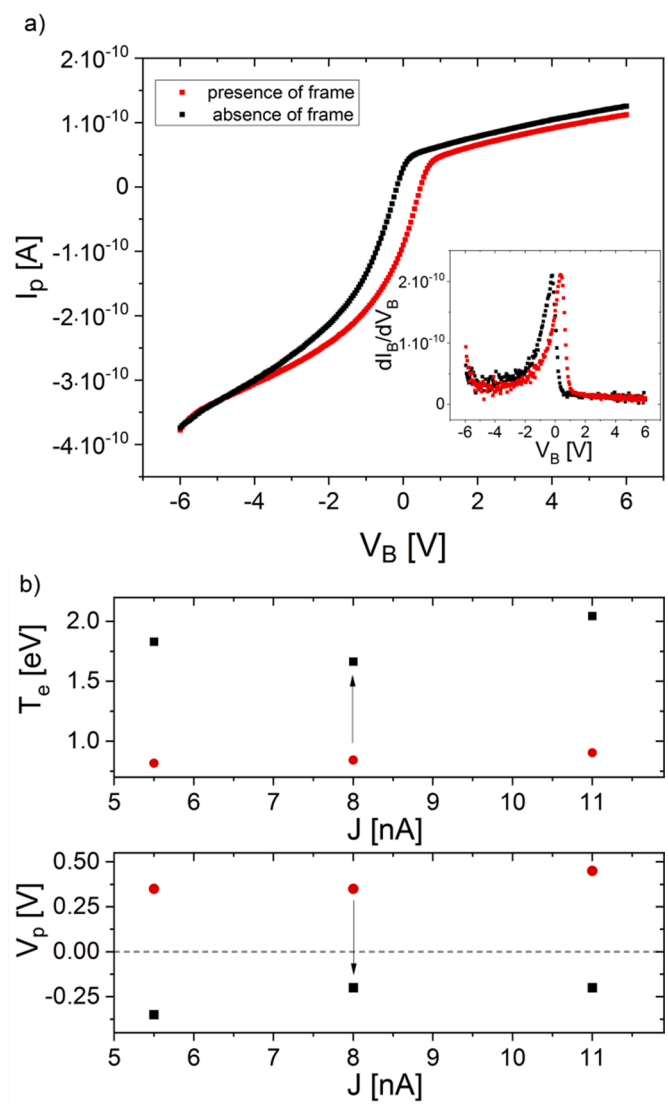

Fig. 12. (a) The measured IV curves in presence and absence of the holder frame shown for Ar at a pressure of about 100 Pa and 8 nA beam current. Inset: First derivative of the IV curves showing that the plasma potential shifts from +0.35 V towards −0.19 V in the absence of the frame. (b) Effect of the frame on electron temperatures determined by the ln-slope method and plasma potential.

regime and modified slopes in both saturation regimes are visible, thus affecting the determined T_e.

A negative floating potential is expected in Ar plasmas in the studied parameter range, since it reflects the higher velocity of electrons compared to ions. We thus attribute the observation of a positive V_f in experiments with the frame to a potential shift from the positive biasing of the frame due to incomplete plasma shielding.

In contrast, the observed negative plasma potential after frame removal is rather unconventional. Generally, negative plasma potentials can emerge if loss rates of the positive species exceed those of the negative species. Since the electron current in the saturation regime is almost unchanged (SI 3), the shift of electron saturation onset to slightly negative potentials cannot be explained by a reduced electron density. However, an increase of the high energy tail of the EEDF that is too small to contribute to the electron current might explain a negative V_p, as shown by Oksuz et al. [65]. They studied an unmagnetized DC argon plasma with plasma parameters of $T_e \sim 0.3$ eV and n_i of $5*10^{11} m^{-3}$, and $\lambda_D \sim 6$ mm, rather similar to the ETEM conditions. The observed negative plasma potential in [65] reveals that high energy primary electrons can lead to a modified double layer at a metal plate, where electrons can be confined at a negative V_p. Analogously, in our setup, trapping of energetic electrons might occur near the pole pieces.

In our experiment, the 300 keV electrons from the primary beam mainly undergo forward scattering in the gas. Thus, they do not contribute to potentials at the walls nor do they impinge the TEM holder. However, secondary electrons with a high energy tail at energies $E_{kin} \gg T_e$ are present, as visible in the EELS spectra (S1 of the SI). These can redistribute the potential distribution in order to maintain quasi-neutrality. The presence of the frame can give rise to additional scattering of these high energy SE's. This would imply that the sheath situation in the ETEM plasma is more complex than assumed by the OML theory: Due to the large Debye lengths, the sheaths at the pole piece wall and around the probe are overlapping. This in turn implies that in the ETEM geometry the Langmuir probe is probing a strongly depleted plasma that is located in the overlapping space charge layers of the two pole piece walls and further modified by the frame and the probe.

A proper test of this theory requires experimentally challenging spatially resolved measurements of the plasma potential and may be subject of further investigations in order to clarify the particular sheath situation in the ETEM. As a first step, we have compared Langmuir probe measurements as a function of the distance between the primary electron beam and the probe tip. We observe that the I-V characteristic is almost independent of the beam - probe tip distance in a range between 60 and 350 μm within the sample plane. This confirms that the plasma is rather homogeneous in the x-y plane, in agreement with the large determined values of λ_D and λ_{mfp} of the electrons. Clearly, the measured range of the x-y plane covers only a fraction of the in-plane plasma extension. However, it is the relevant one for ETEM experiments. In contrast, the plasma parameters should rather strongly depend on the z-direction due to the formation of the space charge layer perpendicular to the pole piece surfaces, since these are the closest surfaces to the Langmuir probe.

5.3. Critical evaluation of the results and applicability of the Langmuir theory

Regardless of these concerns, our analysis suggests that the plasma parameters as determined in the previous chapters monitor at least effective values for the particular plasma state at the position of a TEM sample. In order to critically evaluate the applicability of the OML model and determine effective parameters, in the following, we review the individual Langmuir requirements:

Cold ions: T_i / $T_e \ll 1$. Since the ion thermal energy cannot be derived from Langmuir measurements, we have no experimental access to this condition. However, the ratio of momentum transfer scales inversely to the particle mass ratio. Thus, there is no reason to doubt this condition.

Energy distribution of electrons at or near thermal equilibrium. This condition was checked experimentally with the generalized Gudmundssen fits. The EEDF can be considered as Maxwellian within the 95%-confidence interval for the majority of evaluated datasets. The presence of a high energy tail at $E >> T_e$ as visible in the EELS analysis cannot be determined by the current-voltage characteristics since their contribution is too small. However, these high energy electrons might influence the potential distribution at open circuit conditions, i.e. at low currents.

Collision-less plasma: An ideal plasma is collision-less, which implies that charged-neutral collisions dominate over coulomb collisions. Therefore, collective behaviour of the charge carriers with the formation of sheath layers at conducting walls is expected in agreement with our observation. According to [66], the criterion for non-ideal plasma is given by the parameter γ:

$$\gamma = Z \cdot e^2 \cdot n_0^{1/3} \cdot T_e^{-1} \ll 1 \tag{14}$$

The γ parameter describes the ratio between characteristic potential energy of the coulomb interaction over the mean interparticle distance, and the mean thermal energy. If we apply this formula with the values from the limiting case approximations, we obtain $\gamma_{Ar} = 2.0 \cdot 10^{-15}$ and $\gamma_{He} = 1.2 \cdot 10^{-26}$. Therefore, we can consider the plasma as collision-less outside the generation volume due to the very low charge carrier density.

Electrostatic plasma: The plasma is generated by a dc primary electron beam. AC electric fields are avoided in the electrostatic lens systems of the TEM in order to maintain high stability of imaging. Consequently, the plasma type is electrostatic. Furthermore, a rather slow voltage sweep of 12.5 mV/s is chosen for the acquisition of the I-V curves.

Non-magnetized: The experiments are performed in the Lorentz mode of the microscope, where the magnetic stray field of the objective lens at the position of the TEM holder is strongly reduced to a small residual magnetic field in the order of 10 mT. Difficulties arise when quantifying the exact magnitude, due to magnetic hysteresis and variance in power supply conditions [67]. The Larmor radius for an electron with energy of $T_e = 0.4$ eV at 10 mT external field is with 213 μm comparable to the wire radius. Thus, we expect a distortion of the electron current. In contrast, the Larmor radius for ions is a factor of m_i/m_e times larger and therefore the condition is fulfilled at least for the ion-saturation regime. Preliminary experiments in μ-probe mode with a different TEM holder indicate a 3-fold reduction of electron saturation current in large magnetic fields (SI 4). This suggests that the magnetic field is not the main origin of the very large reduction of electron saturation currents in our Langmuir setup. Despite some steps towards modelling of magnetic field effects e.g. in Ref. [68], the appropriate quantitative modelling for the electron current reduction factor is challenging and out of the scope of this work.

Quasi-neutrality conditions $n_i \approx n_e$: This condition is typically preserved in bulk plasmas, where the sheath at surfaces is formed to maintain the charge neutrality in the bulk. Within the sheath layer, this condition is typically violated. The overlapping sheath regions of the two pole piece surfaces may thus be the major reason that the observed ratio between electron and ion saturation current is far below the expected value for both gas species.

Isotropy and Homogeneity: Both conditions are violated due to the local generation of ions in the interaction volume of the primary electrons with the gas that has a close to cylindrical geometry. In addition, the flat gap geometry of the two conducting pole piece surfaces that confine the plasma will induce an anisotropic sheath layer. We assume that at a certain distance from the beam area a plasma state is formed that is rather homogeneous in the x-y plane. Indeed, a reference measurement with a tip-beam distance of 350 μm differs only by 13% from the ion density results at a distance of 50 μm. However, along the z-

direction, the spatial properties are determined by the overlapping sheath layers perpendicular to both pole piece surfaces. In order to estimate to what degree the measured ion density is depleted, in the following it is compared to an ion density estimate derived from

$$\frac{\partial n_{ion}}{\partial t} = c_{gas}\sigma_{ion}n_e v - n_{ion}\left[\frac{1}{\tau_s}+\frac{1}{\tau_{cap}}\right]. \tag{15}$$

Here, the ion generation is determined by $\frac{j}{e} = n_e v$ with the primary electron current j, ionisation cross section σ_{ion}($0.9{\cdot}10^{-20}$ m^2 for Ar [52] and $0.1{\cdot}10^{-20}$ m^2 for He [69], both at 1 keV) and pressure dependent volume density of gas atoms c_{gas}. The ion depletion is mainly determined by the charged particle loss time τ_s due to surface adsorption. For a bulk plasma, the charged particle loss time follows from the Bohm velocity and the characteristic linear dimension $\tau_s = d_s\sqrt{\frac{e\ m_{ion}}{k_B T_e}}$. The upper limit is $2.8{\cdot}\ 10^{-9}$ s at the maximum distance of $d_s = 2.7$ mm to both surfaces in the centre of the pole piece gap. This entirely dominates over the electron capture time τ_{cap}. For Ar it varies between 1 s and 1 ms in the pressure range between 0.1 Pa and 500 Pa, based on an electron capture cross section $\sigma_{capt} = 10^{-20}$ m^2 [70]. For He, it is between 330 ms and 0.33 ms for $\sigma_{capt} = 3{\cdot}10^{-20}$ m^2 [71]. In the stationary state, Eq. (15) yields

$$n_{ion} = c_{gas}\sigma_{ion}\frac{j}{e}\left[\frac{1}{\tau_s}+\frac{1}{\tau_{cap}}\right]^{-1} \tag{16}$$

giving an ionisation ratio of $6.2{\cdot}10^{-7}$ both for Ar and He in a bulk plasma. Thus, the estimated ion density is about 5 orders of magnitude above the measured one. Our approximate calculation can only give an upper limit, since it does not take into account that d_s varies in the cylindrical ion generation volume, and that our measurement takes place in the sheath layer. Nevertheless, the charged particle loss time τ_s at surfaces totally dominates the plasma situation. We thus conclude that our Langmuir probe measures a strongly depleted ion density within the sheath layer.

EEDF consistency: Criteria to check whether the Langmuir probe can disturb the EEDF due to size effects have been formulated by Godyak et al. [72]. The detailed analysis is given in SI 5. It shows that, not only the pole piece surface but also the probe disturbs the plasma, due to the large electron Debye lengths in the ETEM plasma. Consequently, both for He and for Ar at higher pressures, the small probe assumption is violated. Waymouth [73] gave criteria for the distortion of the EEDF due to probe induced drain of the plasma. Our analysis in appendix B shows that both noble gases violate the Waymouth criterion due to the small plasma volume and the low plasma densities. The violation of the Waymouth criterion should mainly distort the high energy tail of the EEDF. Furthermore, the circuit resistance of the Langmuir setup can disturb the low energy region of the EEDF since it affects the current-voltage curve near the plasma potential [74]. As shown in SI 5 of the SI, our measurement circuit fulfills the criteria.

6. Summary and conclusions

In-situ Langmuir-probe measurements in the ETEM provide important insights into the ionization state of two selected noble gases for the typical electron beam settings for imaging and accessible pressure ranges between 0.1 Pa and 500 Pa. Qualitatively the experimental Langmuir characteristics coincide well with the theoretical OML prediction. In particular, the existence of saturation- and retarding regimes demonstrates that the charge carriers exhibit collective behaviour, the characteristics of a plasma. This implies that a space charge region exists in the ETEM plasma state, a sheath layer, and that conventional plasma descriptors can be used to a certain degree. The strong difference between the experimental and theoretical ratio for the electron and ion saturation currents indicates that the small plasma volume confined in a 5.4 mm pole piece gap with conducting surfaces has a strong impact on the plasma state. Furthermore, the residual magnetic field that may still be present in the Lorentz mode can further disturb the electron branch due to the resulting Larmor radius. For this reason, the ion-current has been used for the analysis in this paper. The resulting ionization ratio of about $6{\cdot}10^{-12}$ is much smaller than theoretical prediction of $6{\cdot}10^{-7}$ in the interaction volume of the electron beam with the gas. This strong ion and electron depletion at the probe position is fully consistent with our observation that the Debye length strongly exceeds the vertical extension of the plasma in the pole piece gap.

Contrary to the expectation of a strongly distorted EEDF at the probe position in the double sheath layer of the two pole piece surfaces, the reconstructed EEDFs have exceptional good quality and show a near Maxwellian distribution. Their shapes do not seem to be disturbed in the low energy region and should be reliable according to the relevant tests. In particular, the determined electron plasma temperature T_e based on OML theory is roughly consistent with the EEDF.

Consequently, the plasma parameters determined by the OML theory describe effective values of the plasma within the sheath layer, with orders of magnitude depleted ion and electron densities. These results are valuable for *in-situ* ETEM experiments in gases in order to understand the effect of electron impact ionization on observed nanoscale behaviour of catalysts, surfaces and processes in chemical reactions. We conclude that ion and electron densities due to direct beam interaction with the gas are rather small compared to the effects that occur when a beam is placed on a TEM lamella. Assuming the same atomic ionization cross section, the SE generation at the solid surface of a TEM lamella exceeds the SE generation in the gas by the atom density ratio, i.e. a factor of 10^6–10^2 in the pressure range of 100 Pa - 500 Pa. Nevertheless, the measurement of ETEM plasma parameters by a Langmuir probe enables access to ion and electron properties induced by beam-gas interactions and thus allows for their consideration *in-situ* environmental experiments. In particular, for catalytically or electrochemically active specimens, the reaction pathways can be altered by the plasma. Furthermore, the interpretation of many *in-situ* gas observations such as nanowire growth, nanoparticle morphology change, oxidation or reduction of materials can be significantly influenced by the insight that the gas undergoes the transition into a dilute plasma state under electron illumination.

The logical follow-up work would contain the Langmuir characterization of reactive gases and complex molecules. This leads to the challenge to distinguish between different positive ion species or to separate the electron current from negative ion-currents. A promising separation candidate could be the EEDF. Since this work has shown the applicability of plasma diagnostics in the ETEM, this and further techniques can be implemented in the future to study other gases.

Declaration of Competing Interest

The authors declare that they have no known competing financial interests or personal relationships that could have appeared to influence the work reported in this paper.

Data Availability

Data will be made available on request.

Acknowledgments

This work is funded by the Deutsche Forschungsgemeinschaft (DFG, German Research Foundation) 217133147/SFB 1073, projects C02 and Z02. Use of equipment in the “Collaborative Laboratory and User Facility for Electron Microscopy” (CLUE) at University of Goettingen is gratefully acknowledged. We thank M. Hahn and the mechanical workshop of the Physics Faculty very much for the construction of the Langmuir probe. We gratefully acknowledge valuable discussion with Andrew Gibbson, Moritz Oberberg and Peter Awakowicz, University of

Bochum about the plasma analysis.

Supplementary materials

Supplementary material associated with this article can be found, in the online version, at doi:10.1016/j.ultramic.2022.113629.

References

[1] Y.A. Wu, L. Li, Z. Li, A. Kinaci, M.K.Y. Chan, Y. Sun, J.R. Guest, I. McNulty, T. Rajh, Y. Liu, Visualizing redox dynamics of a single Ag/AgCl heterogeneous nanocatalyst at atomic resolution, ACS Nano 10 (2016) 3738–3746.

[2] R. Arrigo, M. Hävecker, M.E. Schuster, C. Ranjan, E. Stotz, A. Knop-Gericke, R. Schlögl, *In situ* study of the gas-phase electrolysis of water on platinum by NAP-XPS, Angew. Chem. Int. Ed. 52 (2013) 11660–11664.

[3] S. Zhang, L. Nguyen, Y. Zhu, S. Zhan, C.K. Tsung, F. Tao, *In-situ* studies of nanocatalysis, Acc. Chem. Res. 46 (2013) 1731–1739.

[4] Y. Li, D. Zakharov, S. Zhao, R. Tappero, U. Jung, A. Elsen, P. Baumann, R.G. Nuzzo, E.A. Stach, A.I. Frenkel, Complex structural dynamics of nanocatalysts revealed in Operando conditions by correlated imaging and spectroscopy probes, Nat. Commun. 6 (2015) 7583, https://doi.org/10.1038/ncomms8583.

[5] M.A. Banares, I.E. Wachs, Molecular structures of supported metal oxide catalysts under different environments, J. Raman Spectrosc. 33 (2002) 359–380, https://doi.org/10.1002/jrs.866.

[6] J. Wu, H. Shan, W. Chen, X. Gu, P. Tao, C. Song, W. Shang, T. Deng, *In situ* environmental TEM in imaging gas and liquid phase chemical reactions for materials research, Adv. Mater. 28 (2016) 9686–9712.

[7] M.W. Kanan, D.G. Nocera, *In situ* formation of an oxygen-evolving catalyst in neutral water containing phosphate and Co^{2+}, Science (80-.) 321 (2008) 1072–1075, https://doi.org/10.1126/science.1162018.

[8] D.A. Lutterman, Y. Surendranath, D.G. Nocera, A self-healing oxygen-evolving catalyst, J. Am. Chem. Soc. 131 (2009) 3838–3839.

[9] Y. Jiang, H. Li, Z. Wu, W. Ye, H. Zhang, Y. Wang, C. Sun, Z. Zhang, *In situ* observation of hydrogen-induced surface faceting for palladium–copper nanocrystals at atmospheric pressure, Angew. Chem. Int. Ed. 55 (2016) 12427–12430.

[10] H. Yoshida, Y. Kuwauchi, J.R. Jinschek, K. Sun, S. Tanaka, M. Kohyama, S. Shimada, M. Haruta, S. Takeda, Visualizing gas molecules interacting with supported nanoparticulate catalysts at reaction conditions, Science (80-.) 335 (2012) 317–319.

[11] B.K. Miller, T.M. Barker, P.A. Crozier, Novel sample preparation for operando TEM of catalysts, Ultramicroscopy 156 (2015) 18–22.

[12] P.E. Batson, N. Dellby, O.L. Krivanek, Sub-ångstrom resolution using aberration corrected electron optics, Nature 418 (2002) 617–620, https://doi.org/10.1038/nature00972.

[13] P.D. Nellist, M.F. Chisholm, N. Dellby, O.L. Krivanek, M.F. Murfitt, Z.S. Szilagyi, A. R. Lupini, A. Borisevich, W.H. Sides, S.J. Pennycook, Direct sub-angstrom imaging of a crystal lattice, Science (80-.) 305 (2004) 1741, https://doi.org/10.1126/science.1100965.

[14] K.W. Urban, Studying atomic structures by aberration-corrected transmission electron microscopy, Science (80-.) 321 (2008) 506–510.

[15] M. Haider, S. Uhlemann, E. Schwan, H. Rose, B. Kabius, K. Urban, Electron microscopy image enhanced, Nature 392 (1998) 768–769, https://doi.org/10.1038/33823.

[16] M.A. Haque, M.T.A. Saif, Application of MEMS force sensors for *in situ* mechanical characterization of nano-scale thin films in SEM and TEM, Sens. Actuators A Phys. 97 (2002) 239–245.

[17] S. Lu, D.A. Dikin, S. Zhang, F.T. Fisher, J. Lee, R.S. Ruoff, Realization of nanoscale resolution with a micromachined thermally actuated testing stage, Rev. Sci. Instrum. 75 (2004) 2154–2162, https://doi.org/10.1063/1.1710703.

[18] Y. Zhu, N. Moldovan, H.D. Espinosa, A microelectromechanical load sensor for *in situ* electron and x-ray microscopy tensile testing of nanostructures, Appl. Phys. Lett. 86 (2005) 13506, https://doi.org/10.1063/1.1844594.

[19] M.A. Haque, H.D. Espinosa, H.J. Lee, MEMS for *in situ* testing-handling, actuation, loading, and displacement measurements, MRS Bull. 35 (2010) 375–381.

[20] L.F. Allard, W.C. Bigelow, M. Jose-Yacaman, D.P. Nackashi, J. Damiano, S.E. Mick, A new MEMS-based system for ultra-high-resolution imaging at elevated temperatures, Microsc. Res. Tech. 72 (2009) 208–215.

[21] J.F. Creemer, S. Helveg, P.J. Kooyman, A.M. Molenbroek, H.W. Zandbergen, P. M. Sarro, A MEMS reactor for atomic-scale microscopy of nanomaterials under industrially relevant conditions, J. Microelectromech. Syst. 19 (2010) 254–264, https://doi.org/10.1109/JMEMS.2010.2041190.

[22] L.F. Allard, S.H. Overbury, W.C. Bigelow, M.B. Katz, D.P. Nackashi, J. Damiano, Novel MEMS-based gas-cell/heating specimen holder provides advanced imaging capabilities for *in situ* reaction studies, Microsc. Microanal. 18 (2012) 656, https://doi.org/10.1017/S1431927612001249.

[23] F. Wu, N. Yao, Advances in windowed gas cells for *in-situ* TEM studies, Nano Energy 13 (2015) 735–756.

[24] S.B. Vendelbo, C.F. Elkjær, H. Falsig, I. Puspitasari, P. Dona, L. Mele, B. Morana, B. J. Nelissen, R. Van Rijn, J.F. Creemer, Visualization of oscillatory behaviour of Pt nanoparticles catalysing CO oxidation, Nat. Mater. 13 (2014) 884–890.

[25] S.A. Freunberger, Y. Chen, Z. Peng, J.M. Griffin, L.J. Hardwick, F. Bardé, P. Novák, P.G. Bruce, Reactions in the rechargeable lithium–O2 battery with alkyl carbonate electrolytes, J. Am. Chem. Soc. 133 (2011) 8040–8047.

[26] S. Muto, S. Arai, T. Higuchi, K. Orita, S. Ohta, H. Tanaka, T. Suganuma, M. Ibe, H. Hirata, Environmental high-voltage S/TEM combined with a quadrupole mass spectrometer for concurrent *in situ* structural characterization and detection of product gas molecules associated with chemical reactions, Microscopy 68 (2019) 185–188.

[27] A. Wittstock, V. Zielasek, J. Biener, C.M. Friend, M. Bäumer, Nanoporous gold catalysts for selective gas-phase oxidative coupling of methanol at low temperature, Science (80-.) 327 (2010) 319–322.

[28] J. Wu, W. Gao, H. Yang, J.M. Zuo, Dissolution kinetics of oxidative etching of cubic and icosahedral platinum nanoparticles revealed by *in situ* liquid transmission electron microscopy, ACS Nano 11 (2017) 1696–1703.

[29] S.B. Simonsen, I. Chorkendorff, S. Dahl, M. Skoglundh, J. Sehested, S. Helveg, Ostwald ripening in a Pt/SiO2 model catalyst studied by *in situ* TEM, J. Catal. 281 (2011) 147–155.

[30] S. Dai, Y. Hou, M. Onoue, S. Zhang, W. Gao, X. Yan, G.W. Graham, R. Wu, X. Pan, Revealing surface elemental composition and dynamic processes involved in facet-dependent oxidation of Pt3Co nanoparticles via *in situ* transmission electron microscopy, Nano Lett. 17 (2017) 4683–4688.

[31] F. Tao, M.E. Grass, Y. Zhang, D.R. Butcher, J.R. Renzas, Z. Liu, J.Y. Chung, B. S. Mun, M. Salmeron, G.A. Somorjai, Reaction-driven restructuring of Rh-Pd and Pt-Pd core-shell nanoparticles, Science (80-.) 322 (2008) 932–934.

[32] S. Raabe, D. Mierwaldt, J. Ciston, M. Uijttewaal, H. Stein, J. Hoffmann, Y. Zhu, P. Blöchl, C. Jooss, *In situ* electrochemical electron microscopy study of oxygen evolution activity of doped manganite perovskites, Adv. Funct. Mater. 22 (2012) 3378–3388.

[33] S. Mildner, M. Beleggia, D. Mierwaldt, T.W. Hansen, J.B. Wagner, S. Yazdi, T. Kasama, J. Ciston, Y. Zhu, C. Jooss, Environmental TEM study of electron beam induced electrochemistry of Pr0. 64Ca0. 36MnO3 catalysts for oxygen evolution, J. Phys. Chem. C 119 (2015) 5301–5310.

[34] T.W. Hansen, J.B. Wagner, Controlled Atmosphere Transmission Electron Microscopy, Springer Int. Publ, Switz, 2016, pp. 213–235, https://doi.org/10.1007/978-3-319-22988-1.

[35] H.L. Xin, E.A. Pach, R.E. Diaz, E.A. Stach, M. Salmeron, H. Zheng, Revealing correlation of valence state with nanoporous structure in cobalt catalyst nanoparticles by *in situ* environmental tem, ACS Nano 6 (2012) 4241–4247.

[36] D. Mierwaldt, V. Roddatis, M. Risch, J. Scholz, J. Geppert, M.E. Abrishami, C. Jooss, Environmental TEM investigation of electrochemical stability of perovskite and ruddlesden–popper type manganite oxygen evolution catalysts, Adv. Sustain. Syst. 1 (2017), 1700109.

[37] G. Lole, V. Roddatis, U. Ross, M. Risch, T. Meyer, L. Rump, J. Geppert, G. Wartner, P. Blöchl, C. Jooss, Dynamic observation of manganese adatom mobility at perovskite oxide catalyst interfaces with water, Commun. Mater. 1 (2020) 1–10, https://doi.org/10.1038/s43246-020-00070-6.

[38] M. Bugnet, S.H. Overbury, Z.L. Wu, T. Epicier, Direct visualization and control of atomic mobility at ${$100$}$ surfaces of ceria in the environmental transmission electron microscope, Nano Lett. 17 (2017) 7652–7658.

[39] W. Yuan, Y. Wang, H. Li, H. Wu, Z. Zhang, A. Selloni, C. Sun, Real-time observation of reconstruction dynamics on TiO_2 (001) surface under oxygen via an environmental transmission electron microscope, Nano Lett. 16 (2016) 132–137.

[40] R. Sharma, Design and applications of environmental cell transmission electron microscope for *in situ* observations of gas–solid reactions, Microsc. Microanal. 7 (2001) 494–506.

[41] J.R. Jinschek, S. Helveg, Image resolution and sensitivity in an environmental transmission electron microscope, Micron 43 (2012) 1156–1168.

[42] V.I. Pârvulescu, M. Magureanu, P. Lukes, Plasma Chemistry and Catalysis in Gases and Liquids, John Wiley & Sons, 2012.

[43] Y.F. Guo, D.Q. Ye, K.F. Chen, J.C. He, W.L. Chen, Toluene decomposition using a wire-plate dielectric barrier discharge reactor with manganese oxide catalyst *in situ*, J. Mol. Catal. A Chem. 245 (2006) 93–100.

[44] A.E. Wallis, J.C. Whitehead, K. Zhang, Plasma-assisted catalysis for the destruction of CFC-12 in atmospheric pressure gas streams using TiO2, Catal. Lett. 113 (2007) 29–33.

[45] A.S. Pribytkov, G.N. Baeva, N.S. Telegina, A.L. Tarasov, A.Y. Stakheev, A. V. Tel`nov, V.N. Golubeva, Effect of electron irradiation on the catalytic properties of supported Pd catalysts, Kinet. Catal. 47 (2006) 765–769, https://doi.org/10.1134/S0023158406050168.

[46] J. Jun, J.C. Kim, J.H. Shin, K.W. Lee, Y.S. Baek, Effect of electron beam irradiation on CO2 reforming of methane over Ni/Al_2O_3 catalysts, Radiat. Phys. Chem. 71 (2004) 1095–1101.

[47] J. Van Durme, J. Dewulf, C. Leys, H. Van Langenhove, Combining non-thermal plasma with heterogeneous catalysis in waste gas treatment: a review, Appl. Catal. B Environ. 78 (2008) 324–333.

[48] J.P.S. Badyal, Catalysis and plasma chemistry at solid surfaces, Top. Catal. 3 (1996) 255, https://doi.org/10.1007/BF02431188.

[49] W.M. Manheimer, R.F. Fernsler, M. Lampe, R.A. Meger, Theoretical overview of the large-area plasma processing system (LAPPS), Plasma Sources Sci. Technol. 9 (2000) 370, https://doi.org/10.1088/0963-0252/9/3/316.

[50] R.F. Fernsler, W.M. Manheimer, R.A. Meger, J. Mathew, D.P. Murphy, R. E. Pechacek, J.A. Gregor, Production of large-area plasmas by electron beams, Phys. Plasmas 5 (1998) 2137–2143, https://doi.org/10.1063/1.872886.

[51] D. Leonhardt, S.G. Walton, R.F. Fernsler, Fundamentals and applications of a plasma-processing system based on electron-beam ionization, Phys. Plasmas 14 (2007) 57103, https://doi.org/10.1063/1.2712424.

[52] H.C. Straub, P. Renault, B.G. Lindsay, K.A. Smith, R.F. Stebbings, Absolute partial and total cross sections for electron-impact ionization of argon from threshold to 1000eV, Phys. Rev. A 52 (1995) 1115, https://doi.org/10.1103/PhysRevA.52.1115.
[53] M.B. Shah, D.S. Elliott, P. McCallion, H.B. Gilbody, Single and double ionisation of helium by electron impact, J. Phys. B At. Mol. Opt. Phys. 21 (1988) 2751, https://doi.org/10.1088/0953-4075/21/15/019.
[54] D.B. Langmuir, E. Stuhlinger, J.J.M. Sellen, Electrostatic Propulsion, American Institute of Aeronautics and Astronautics, 1961. https://epub.uni-regensburg.de/36282/.
[55] R.L. Merlino, Understanding Langmuir probe current-voltage characteristics, Am. J. Phys. 75 (2007) 1078–1085.
[56] U. Stroth, Plasma physics Phenomena, foundations, and applications 2 (2018), https://doi.org/10.1007/978-3-662-55236-0.
[57] H. Martinez, F. Castillo, P.G. Reyes, F.G. Santibanez, Experimental studies on the formation of argon atoms in Ar+–atoms collisions, Int. J. Mass Spectrom. 228 (2003) 107–116.
[58] F.J. De Heer, J. Schutten, H. Moustafa, Ionization and electron capture for helium ions incident on noble and diatomic gases between 10 and 150keV, Physica 32 (1966) 1793–1807.
[59] J.E. Allen, Probe theory - the orbital motion approach, Phys. Scr. 45 (1992) 497–503, https://doi.org/10.1088/0031-8949/45/5/013.
[60] F.F. Chen, J.P. Chang, Lecture Notes on Principles of Plasma Processing, Springer Science & Business Media, 2012.
[61] R.B. Lobbia, B.E. Beal, Recommended practice for use of Langmuir probes in electric propulsion testing, J. Propuls. Power 33 (2017) 566–581, https://doi.org/10.2514/1.B35531.
[62] G.F. Matthews, Tokamak plasma diagnosis by electrical probes, Plasma Phys. Control. Fusion 36 (1994) 1595.
[63] M.J. Druyvesteyn, Der Niedervoltbogen, Z. Phys. 64 (1930) 781–798, https://doi.org/10.1007/BF01773007.
[64] J.T. Gudmundsson, On the effect of the electron energy distribution on the plasma parameters of an argon discharge: a global (volume-averaged) model study, Plasma Sources Sci. Technol. 10 (2001) 76–81, https://doi.org/10.1088/0963-0252/10/1/310.
[65] L. Oksuz, N. Hershkowitz, Negative plasma potential in unmagnetized DC electropositive plasma with conducting walls, Phys. Lett. A 375 (2011) 2162–2165.
[66] V.E. Fortov, I.T. Iakubov, The Physics of Non-Ideal Plasma, World Scientific, 2000.
[67] J. Wild, Lorentz-Transmissionselektronenmikroskopie und Differentielle Phasenkontrastmikroskopie an magnetischen Skyrmionen, 2017.
[68] E.P. Szuszczewicz, P.Z. Takacs, Magnetosheath effects on cylindrical Langmuir probes, Phys. Fluids 22 (1979) 2424–2429, https://doi.org/10.1063/1.862556.
[69] A. Kramida, Yu. Ralchenko, J. Reader, Atomic Spectra Database, (2020). 10.18434/T4W30F.
[70] H. Klinger, A. Müller, E. Salzborn, Electron capture cross sections for multiply charged argon ions passing through nitrogen and krypton targets at energies from 10 to 110keV, J. Chem. Phys. 65 (1976) 3427–3430, https://doi.org/10.1063/1.433595.
[71] H. Schiff, Electron capture cross sections, Can. J. Phys. 32 (1954) 393–405, https://doi.org/10.1139/p54-041.
[72] V.A. Godyak, V.I. Demidov, Probe measurements of electron-energy distributions in plasmas: what can we measure and how can we achieve reliable results? J. Phys. D. Appl. Phys. 44 (2011), 233001.
[73] J.F. Waymouth, Perturbation of electron energy distribution by a probe, J. Appl. Phys. 37 (1966) 4492–4497.
[74] M. Fiebrandt, M. Oberberg, P. Awakowicz, Comparison of Langmuir probe and multipole resonance probe measurements in argon, hydrogen, nitrogen, and oxygen mixtures in a double ICP discharge, J. Appl. Phys. 122 (2017) 13302, https://doi.org/10.1063/1.4991493.